Journal of Materials Chemistry A

ROYAL SOCIETY OF CHEMISTRY

PAPER

View Article Online
View Journal

Check for updates

Cite this: DOI: 10.1039/d5ta09402j

One-pot nanocasting of 3D ordered bicontinuous mesoporous Pt-based multimetallic alloys for efficient hydrogen evolution

Chonghan Xia,†[a] Junhao Ma,†[a] Qihang Chen,[a] Yee Yan Tay,[b] Lydia H. Wong [a] and Kwan W. Tan *[a]

Received 19th November 2025
Accepted 10th March 2026

DOI: 10.1039/d5ta09402j

rsc.li/materials-a

The synthesis of ordered mesoporous multimetallic alloys (MMAs) with controlled composition remains challenging due to disparate reduction kinetics of multimetal precursors. Here we report a one-pot nanocasting approach in which PtFeCoNiCu salts are co-infiltrated and co-reduced within a gyroidal KIT-6 mesoporous silica scaffold, followed by template removal and acid etching, yielding single phase fcc mesoporous alloys with a 3D bicontinuous network morphology. By tuning the reduction conditions, we regulate the incorporation of Fe, Co and Ni around a PtCu-rich solid-solution lattice and remove FeCoNi overgrowths, exposing an ordered Pt-based mesoporous framework with excellent HER performance. The optimized ordered MMA catalyst, delivers an overpotential of 25 mV at 10 mA cm^{-2}, a Tafel slope of 49.1 mV dec^{-1}, and negligible degradation over 100 000 cycles, outperforming both commercial Pt/C and mesoporous Pt controls. This work demonstrates a general route to compositionally tuned ordered mesoporous multimetallic solid-solution alloys suitable for catalysis, sensing and related functional materials.

1 Introduction

Ordered mesoporous multimetallic alloy (MMA) materials have emerged as attractive platforms for essential applications ranging from (electro)catalysis to energy storage and electronic devices.[1–4] Their compositional diversity, tunable atomic ordering (solid solution or intermetallic phases), and periodic nanoarchitectures provide control over electronic structure, synergistic catalytic activity, and active site accessibility.[5,6] In particular, MMAs are promising electrocatalysts for polymer depolymerization and upcycling, as well as the key reactions such as hydrogen evolution reaction (HER), oxygen reduction reaction (ORR), and nitrate reduction reaction (NO_3RR), central to sustainable energy conversion and chemical recycling.[7–12]

In electrocatalysis, the adsorption energies of key intermediates govern activity by linking surface electronic structure to performance through the Sabatier principle and d-band-center theory.[13] Accordingly, optimal catalysts exhibit near-thermoneutral adsorption of intermediates, which can be tuned by alloying elements that modulate the d-band center relative to the Fermi level.[14] Pt is the state-of-the-art catalyst for HER in acidic media attributed to its favorable hydrogen binding energy. However, in alkaline electrolytes, Pt exhibits sluggish kinetics owing to a high energy barrier for water dissociation in the Volmer step and also suffers from limited durability under extended operation. Several studies have demonstrated that alloying Pt with more oxophilic transition metals (*e.g.*, Ni, Co) facilitates the adsorption and removal of hydroxyl intermediates and simultaneously modifies the electronic properties of Pt atoms, leading to enhanced reaction kinetics.[11,15,16] Employing this alloying strategy within ordered mesoporous nanostructures could further enhance electrocatalytic performance by exposing more accessible active sites, shortening ion and electron transport pathways, and facilitating the rapid release of evolved gas bubbles.[7,17]

Typical strategies for synthesizing ordered mesoporous metal structures rely on soft- or hard-templating routes. Earlier works from Wiesner *et al.*[18,19] reported ordered mesoporous Pt and PdAu structures with lamellar, hexagonal and alternating gyroid morphologies, obtained by co-assembling poly(isoprene-*block*-dimethylaminoethylmethacrylate) and poly(isoprene-*block*-styrene-*block*-dimethylaminoethyl methacrylate) block copolymers with ligand-capped metal nanoparticles. However, the reliance on metal-specific linkers increases complexity and limits compositional generality.[18,19] Yamauchi *et al.*[7] reported a one-pot reduction of PtPdRhRuCu/poly(styrene-*block*-ethylene oxide) system, yielding disordered mesoporous nanospheres with Pd-rich core, Rh/Ru-enriched shells, and dispersed Pt/Cu. The observed reduction sequence (Pd > Pt ≈ Cu > Rh > Ru) contrasted with the thermodynamic order (Pt > Pd > Rh > Ru >

[a]*School of Materials Science and Engineering, Nanyang Technological University, Singapore 639798, Singapore. E-mail: kwtan@ntu.edu.sg*

[b]*Facility for Analysis, Characterization, Testing and Simulation, Nanyang Technological University, Singapore 639798, Singapore*

† These authors contribute equally to the work.

Cu), underscoring the challenge of controlling reduction kinetics in multimetal co-reduction, which could lead to uncontrolled nucleation and phase segregation.[20]

Hard templating using ordered mesoporous silica (*e.g.*, KIT-6) offers a robust path to preserve mesostructural order while enabling multimetal alloy formation.[21,22] Using KIT-6 with a double gyroid framework as the template, Liu *et al.* produced ordered Pt-based intermetallic alloys, including PtSn, PtZnCo, and PtPdFeCoNi.[12,23,24] However, the current approach required preforming Pt within KIT-6, followed by sequential impregnation and reduction of secondary metals, prolonging synthesis and restricts scalability beyond five-metal systems.[21]

In this study, we developed a generalized one-pot templating-reduction strategy to generate ordered PtFeCoNiCu MMAs with a 3D bicontinuous cubic architecture, employing KIT-6 as a hard template and $NaBH_4$ (SBH) as the reducing agent. Mixed metal precursors were co-infiltrated into the KIT-6 mesopores and simultaneously reduced under controlled SBH concentrations (0.25–1.0 M), yielding quinary ordered MMAs. The excessive surface growth of transition metal shells, arising from galvanic exchange and subsequent re-reduction at higher SBH concentrations, was removed by acid washing without disrupting the mesostructural order. The resultant MMAs exhibited excellent HER activity in alkaline media, achieving a low overpotential of 25 mV at 10 mA cm^{-2} and excellent stability over 100 000 cyclic voltammetry sweeps, outperforming the commercial Pt/C control catalyst. The enhanced performance is attributed to the high accessibility of Pt-rich active sites and the effective ion- and electron-transport pathways imparted by the ordered 3D network.

2 Experimental section

2.1 Chemicals and materials

All chemicals were used as received. Potassium tetrachloroplatinate(II) (K_2PtCl_4, ≥99.9% trace metals basis), iron(III) chloride ($FeCl_3 \cdot 6H_2O$, reagent grade, 97%), nickel(II) chloride hexahydrate ($NiCl_2 \cdot 6H_2O$, ACS reagent, 98%), cobalt(II) chloride hexahydrate ($CoCl_2 \cdot 6H_2O$, ReagentPlus), copper(II) chloride dihydrate ($CuCl_2 \cdot 2H_2O$, reagent grade), sodium borohydride ($NaBH_4$, SBH, 99.99% trace metals basis), Pluronic P123 (average Mn ~5800, PEO_{20}-PPO_{70}-PEO_{20}, 99%), *n*-butanol (99.4%), and tetraethyl orthosilicate (TEOS, reagent grade, 98%) were obtained from Sigma-Aldrich. Hydrochloric acid fuming (HCl, 37%) was purchased from Supelco. Nitric acid (HNO_3, 70 wt%) was supplied by Honeywell. Sodium hydroxide (NaOH, 98%) and potassium hydroxide (KOH, 99.99%) were supplied by Aladdin. Hydrogen peroxide (H_2O_2, 30 wt%) was supplied by Qrec. Commercial 20 wt% Pt on Vulcan XC-72R (carbon), Vulcan XC-72 carbon and hydrophilic carbon paper (Toray H-060) were obtained from Fuel Cell Earth.

2.2 Preparation of KIT-6 template

The KIT-6 hybrid was prepared according to previously reported protocols.[25] For a typical synthesis, 1.50 g of Pluronic P123 was dissolved in 54 mL of distilled water and 2.34 mL of HCl solution (37 wt%) under vigorous stirring for about 1 h. After the complete dissolution, 1.853 mL of *n*-butanol was added under stirring at 35 °C for 1 h in a water bath. 3.225 g of TEOS was then added forming a homogeneous clear solution. The mixture was further stirred for 24 h at 35 °C in a water bath. Subsequently, the mixture was hydrothermally heated for 24 h at 100 °C under static conditions in a closed polypropylene bottle. The solid product was centrifuged without washing and dried at 80 °C overnight.

To enhance the hydrophilicity of the KIT-6 silica surface, a gentle oxidation method was introduced using an HNO_3 and H_2O_2 solution at 80 °C to remove the copolymer template. Typically, 1.6 g of the KIT-6 powder was dispersed in a solution containing 24 mL of HNO_3 and 8 mL of H_2O_2 in a 100 mL flask. Subsequently, this mixture was refluxed at 80 °C for 3 h to oxidize the P123 copolymer. (Caution! The temperature of the mixture should be increased gradually. The strongly corrosive nitrogen oxide gases should be bubbled through an aqueous NaOH solution and handled in a chemical fume hood.) The mesoporous silanol functionalized KIT-6 template was obtained after profuse washing with DI water and then drying at 60 °C overnight.

2.3 Preparation of ordered MMAs

53.3 mg of K_2PtCl_4, 20 mg of $FeCl_3 \cdot 6H_2O$, 20 mg of $NiCl_2 \cdot 6H_2O$, 20 mg of $CoCl_2 \cdot 6H_2O$, and 20 mg of $CuCl_2 \cdot 2H_2O$ were dissolved in 2.0 mL of water. Subsequently, 200 mg of silanol functionalized KIT-6 was dispersed in the metal salt solution and dried under vacuum. 2.0 mL of freshly prepared $NaBH_4$ solution (0.25–1.0 M) was added dropwise to the precursor/KIT-6 composite to initiate reduction reaction of metal cations. The mixture was stirred at room temperature for 10 h, forming the metal alloy/KIT-6 composite. The alloy/KIT-6 composite was dispersed in the 2 M NaOH solution under ultrasonication to remove the silica template. Finally, the resultant mesoporous alloy samples were stirred in 1 M HCl for 1 h at room temperature to remove the overgrown surface features. After centrifugation, the solid product was washed with DI water until the pH of the supernatant became neutral, followed by washing with ethanol and drying under vacuum at room temperature. The HCl washing procedure was repeated two additional times.

2.4 Characterization

Small-angle X-ray scattering (SAXS) measurements were performed using a Xenocs NanoinXider instrument in transmission mode using Cu Kα radiation source and Dectris Pilatus 3 detectors. Baseline removal was performed on the integrated SAXS intensity profiles using a smoothing spline fit to the data outside the peak region implemented in OriginPro software. X-ray diffraction (XRD) measurements were performed on a XRD Rigaku SmartLab 3 kW XSPA instrument using Cu Kα radiation source and equipped with XSPA detectors. X-ray photoelectron spectroscopy (XPS) measurements were conducted using an AXIS Supra spectrometer (Kratos Analytical, UK) equipped with a hemispherical analyzer and a monochromatic Al Kα source (1487 eV) operating at 15 mA and 15 kV. The XPS data were

obtained from an analysis area of 700 × 300 μm^2 at a take-off angle of 90°. Pass energies of 160 and 20 eV were used for survey and high resolution scans, respectively, with a 3.1 V bias applied to prevent charge build-up on the samples. Scanning electron microscopy (SEM) images were taken on a JEOL 7600F field emission scanning electron microscope equipped with a half-in-lens detector. The samples were mounted on carbon tape for SEM characterization. Transmission electron microscopy (TEM), selected area electron diffraction (SAED), high-angle annular dark field scanning TEM (HAADF-STEM), and energy-dispersive spectroscopy (EDS) were conducted using a JEOL-2100F electron microscope operating at 200 kV, equipped with a Gatan Ultrascan 1000XP CCD camera, Gatan Digiscan and STEM detectors, and an EDAX EDS detector. The EDS mapping was obtained with a windowless 100 mm^2 Oxford Ultim Max Silicon Drift Detector. Inductively coupled plasma optical emission spectroscopy (ICP-OES) was conducted using a Thermo Fisher iCAP6000 ICP emission spectrometer. Sample solutions were measured after filtering through a 0.22 μm filter.

2.5 Working electrode preparation

The ordered MMA catalyst ink was prepared as follows: 1.0 mg of the catalyst and 1.0 mg of Vulcan XC-72 carbon were dispersed in 1.0 mL of a mixed H_2O/ethanol solvent (1 : 2 v/v). 20 μL of Nafion solution was then added and the mixture was ultrasonicated for 1 h to obtain a homogeneous ink. The catalyst ink was drop cast onto carbon paper and dried at room temperature before use. The final mass loading of the metal alloy catalyst on the electrode was ∼40 μg cm^{-2}.

For the preparation of the commercial 20 wt% Pt/C ink, 5.0 mg of catalyst was dispersed in 1.0 mL of the mixed solvent described above, together with 20 μL of Nafion solution. The catalyst ink was drop cast onto carbon paper to yield a dry loading of ∼200 μg cm^{-2} of commercial 20 wt% Pt/C, corresponding to a Pt loading of ∼40 μg_{Pt} cm^{-2}, which is comparable to the metal alloy loading of the acid-treated MMA samples. To prepare electrodes with lower Pt loading, the dry loading of the 20 wt% Pt/C catalyst was reduced to ∼40 μg cm^{-2}, yielding a Pt loading of ∼8 μg_{Pt} cm^{-2}.

2.6 Electrochemical measurements

All electrochemical measurements were performed using the Autolab IMP workstation under ambient conditions with a standard three-electrode configuration. The setup consists of a mesoporous alloy sample as the working electrode, graphite as the counter electrode, and a calibrated Hg/HgO electrode as the reference electrode. All working electrodes were sandwiched between two pieces of hydrophobic carbon papers to minimize the influence of capillary wetting effects and to isolate them from the platinum clamp holder. To activate the electrocatalysts, the working electrode was subjected to 20 cyclic voltammetry cycles at a scan rate of 100 mV s^{-1} within the potential range of 0.1 to −0.4 V.

All potentials recorded were referenced with respect to the reversible hydrogen electrode (RHE) and *iR*-compensated according to eqn (1),

$$E_{RHE} = E_{Hg/HgO} - E_{offset} - iR \quad (1)$$

where E_{offset} is an experimentally determined conversion factor. It was determined using cyclic voltammetry (CV) on a Pt electrode in an H_2-saturated electrolyte at a scan rate of 10 mV s^{-1} across the hydrogen evolution/oxidation reaction (HER/HOR) potential range. E_{offset} was then calculated by averaging the two zero-current voltage intercepts observed in the CV curve.

Linear sweep voltammetry (LSV) experiments were conducted in an Ar-saturated alkaline aqueous medium (1.0 M KOH) with a scan rate of 5 mV s^{-1}. The overpotential (η) was determined by $\eta = E_{RHE} - 1.23$ (V). The Tafel slope values were determined from the polarization curves using eqn (2),

$$\eta = \left(\frac{2.303RT}{\alpha nF}\right)\log j_0 - \left(\frac{2.303RT}{\alpha nF}\right)\log j \quad (2)$$

where η, j, j_0, α, R, F, n, and T represent the overpotential, current density, exchange current density, charge transfer coefficient, gas constant, Faraday constant, number of charge carriers and temperature, respectively. The Tafel slope values, represented by $2.303RT/\alpha nF$, were determined experimentally obtained by plotting the overpotential η against the logarithm of current density ($\log j$).

Electrochemical impedance spectroscopy (EIS) measurements were performed at −0.1 V over a frequency range from 0.1 Hz to 100 kHz. Electrochemical surface area (ECSA) values were obtained using the hydrogen underpotential deposition (HUPD) method.[17,26] CV measurements were performed at a scan rate of 10 mV s^{-1} in Ar saturated 1.0 M KOH over the potential range of 0.11 to 0.33 V (*vs.* RHE) covering the HUPD region. The baseline-corrected HUPD current was then used to calculate the net faradaic hydrogen adsorption/desorption charge according to eqn (3),

$$Q = \int_{E_1}^{E_2} (i(E) - i_{dl}(E))\frac{dE}{\nu} \quad (3)$$

where Q, E_1, E_2, $i(E)$, $i_{dl}(E)$, and ν represent the net faradaic hydrogen HUPD charge, the integration bounds for the HUPD region, the double-layer baseline current, and the scan rate, respectively. The ECSA was calculated by normalizing Q to the characteristic charge density for a monolayer of adsorbed hydrogen on Pt (0.21 mC cm^{-2}) and to the Pt mass on the electrode (m_{Pt}), according to eqn (4),

$$ECSA = \frac{Q}{0.21\ \text{mC cm}^{-2} \times m_{Pt}} \quad (4)$$

The accelerated durability test (ADT) on the catalysts was performed at a scan rate of 100 mV s^{-1} for over 100 000 cycles of CV in the potential range of 0.1 to −0.3 V (*vs.* RHE).

3 Results and discussion

3.1 Nanocasting of 3D ordered bicontinuous MMAs

Fig. 1a schematically illustrates the synthesis procedure. Ordered mesoporous silica KIT-6, with its double gyroid architecture, served as the hard template. Metal salt precursors were

introduced into the pore network by capillary infiltration during solvent evaporation and reduced with SBH at controlled concentrations, enabling fine modulation of reduction kinetics and alloy composition. The resulting KIT-6/MMA composites were etched with NaOH to remove silica, followed by HCl washing to eliminate surface overgrowth, yielding highly open mesoporous frameworks. The acid-treated samples are denoted MMA-*x*-Acid, where *x* represents the SBH concentration (x = 0.25–1.0 M).

Fig. 1b–d and S1 present scanning electron microscopy (SEM) micrographs of MMA-*x*-Acid samples (x = 0.25–1.0 M), revealing aggregated particles but with a well-defined 3D periodic mesoporous architecture. High-angle annular dark-field scanning transmission electron microscopy (HAADF-STEM) images (Fig. 1e, 2 and S2) further confirm bicontinuous cubic-like mesoporous networks, most pronounced in MMA-0.5-Acid and MMA-0.75-Acid samples. The inverse cubic mesopore arrangement becomes increasingly distinct and interconnected at moderate SBH concentrations, indicating that enhanced reduction strength promotes uniform alloy growth within the KIT-6 mesopore channels and closer replication of its gyroidal network. Mesostructured MMAs were further analyzed by small-angle X-ray scattering (SAXS) to probe ordering over mesoscopic length scales (Fig. S3). The SAXS pattern of the KIT-6 template exhibits a principal peak at $q \approx 0.587$ nm^{-1} and multiple higher-order reflections consistent with an $Ia\bar{3}d$ bicontinuous cubic gyroidal phase. In contrast, the inverse MMA-0.75-Acid sample shows a weaker primary reflection at $q \approx 0.617$ nm^{-1}, together with a broad shoulder at higher q, suggesting a less resolved secondary reflection. The close agreement in the primary peak positions (~4.8%) supports good replication of the KIT-6 mesostructural periodicity. The reduced peak intensity and diminished higher-order features suggest increased disorder and a shorter mesostructural correlation length in the MMA replica, which may arise from interface roughness and partial filling.[18,27] Taken together with TEM and SEM, these SAXS data are consistent with an ordered bicontinuous mesostructure that maintains $Ia\bar{3}d$ type symmetry over finite correlation lengths.

Fig. 1g shows the X-ray diffraction (XRD) patterns of the MMA-*x*-Acid samples series, displaying four well-resolved reflections at 2θ = 40.1°, 47.1°, 68.7°, and 82.6°, corresponding to the (111), (200), (220), and (311) planes of a face-centered cubic (fcc) solid solution phase. These diffraction peak positions closely match those of the PtFeNi alloy (PDF 04-015-0417), which serves as a structural reference for a fcc solid solution lattice. Hence XRD confirmed that all MMA-*x*-Acid samples form a single-phase multimetallic solid solution structure. High-resolution TEM (HRTEM) images in Fig. 1f, S4, and S5 of samples prepared with SBH concentrations ranging from 0.25 to 0.75 M reveal lattice fringes assignable to the (111) and (200) planes of an fcc alloy lattice with interplanar spacings of ~0.22 and 0.20 nm, respectively. The selected area electron diffraction (SAED) pattern of MMA-0.75-Acid in Fig. S6 exhibits diffuse rings decorated with discrete diffraction spots, consistent with a polycrystalline fcc structure.

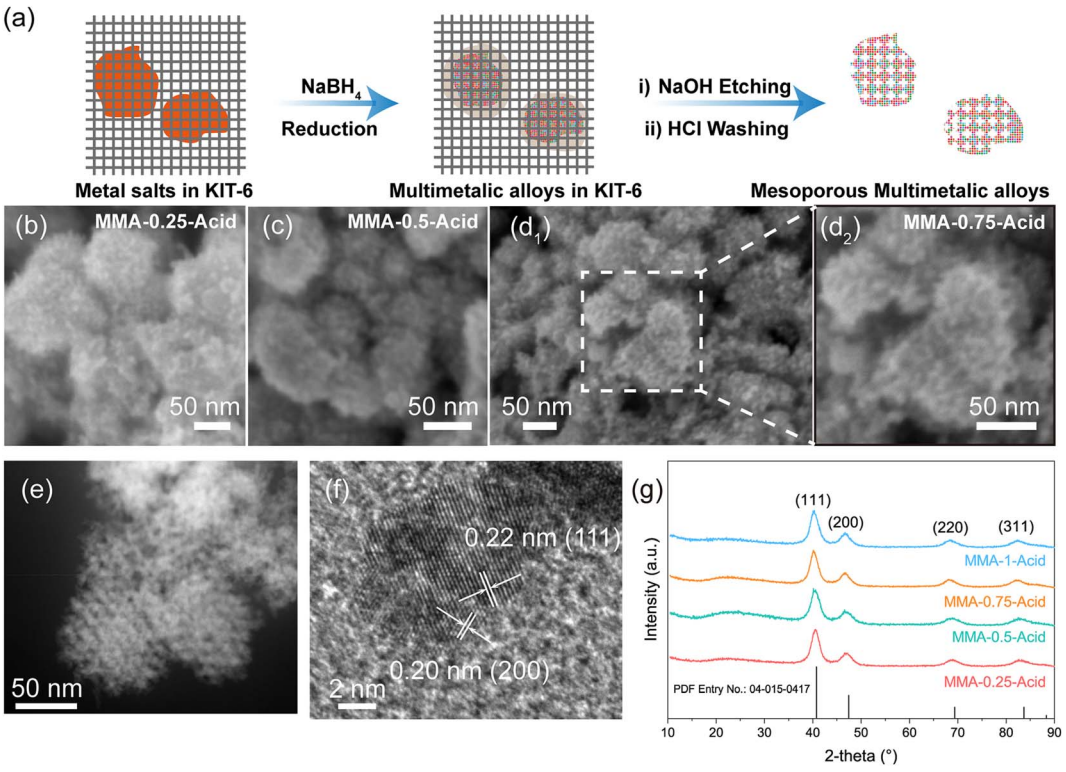

Fig. 1 (a) Schematic illustration of the synthesis of ordered MMAs. SEM of (b) MMA-0.25-Acid, (c) MMA-0.5-Acid, and (d) MMA-0.75-Acid samples. (e) HAADF-STEM of MMA-0.5-Acid. (f) HRTEM of MMA-0.75-Acid. (g) XRD spectra of all MMA-*x*-Acid samples.

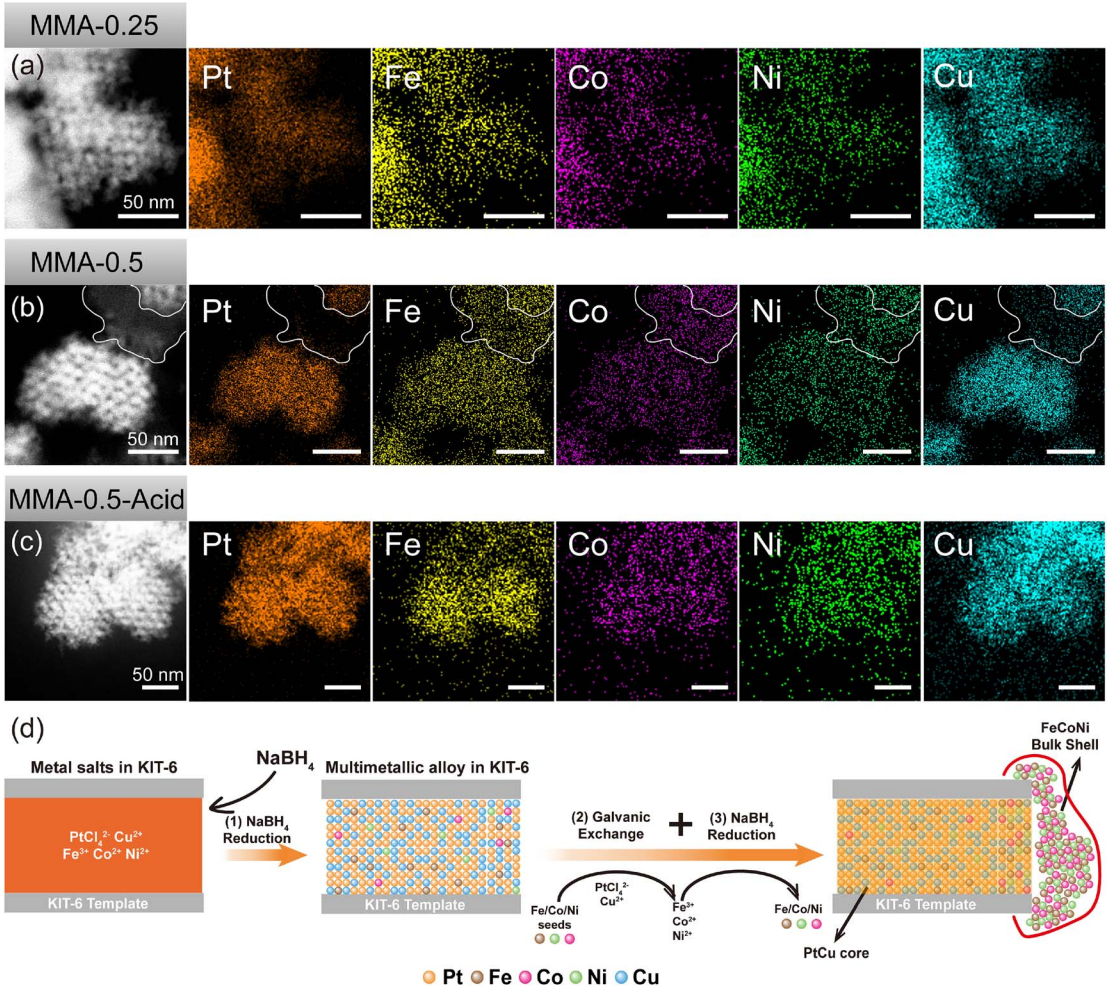

Fig. 2 HAADF-STEM images and corresponding EDS elemental maps of (a) MMA-0.25, (b) MMA-0.5, and (c) MMA-0.5-Acid. (d) Schematic illustration of composition regulation by adjusting SBH concentration.

We further performed energy dispersive spectroscopy (EDS) to investigate how SBH concentration influences the elemental distribution and compositional uniformity within the mesostructure. Fig. 2a, b, S7 and S8 present HAADF-STEM images and corresponding EDS maps of the as-synthesized samples prepared at SBH concentrations of 0.25 and 0.5 M before acid washing. The cubic-like mesoporous morphology of MMA-0.25 indicated that no overgrowth had occurred at low reduction strength. In contrast, at 0.5 M SBH, a distinct bulk-like shell was observed surrounding the mesoporous particles (highlighted in Fig. 2b and S8), suggesting secondary alloy deposition beyond the KIT-6 channels.

EDS mapping in Fig. 2 reveals a relatively uniform distribution of Pt, Fe, Co, Ni, and Cu within the mesoporous frameworks of both MMA-0.25 and MMA-0.5, while the outer shell is enriched in Fe, Co, and Ni (Fig. 2b). Line-profile analyses in Fig. S7 show that both MMA-0.25 and MMA-0.5 samples exhibited a PtCu-rich composition across the mesoporous regions, but MMA-0.5 displayed a notably higher transition metal fraction in the overgrown shell. Similar overgrowth features were observed at higher SBH concentrations (see SEM of MMA-0.75 in Fig. S9). After acid washing, the FeCoNi-rich shells were effectively removed, and the MMA-0.5-Acid sample retained its 3D cubic-like morphology, with EDS signals dominated by Pt and Cu and reduced Fe, Co, and Ni remaining primarily in the mesoporous particle interior (Fig. 2c). HRTEM in Fig. S5b further verifies that acid treatment preserved the polycrystalline fcc lattice of MMA-0.5-Acid, consistent with selective dissolution of the transition metal rich shell without detectable structural degradation.

Fig. 3 presents the EDS line profiles of the ordered MMA particles after acid washing. MMA-0.25-Acid was predominantly Pt-rich (~90 at%) with minor incorporation of Fe, Co, Ni, and Cu (Fig. 3a and b). At an SBH concentration of 0.5 M, Cu and Fe were more uniformly incorporated into the mesoporous alloy (Fig. 3c and d), yielding ~20 at% Cu and ~10 at% Fe. Further increasing the SBH concentration to 0.75 M resulted in greater compositional variation across particles, with enhanced incorporation of Fe, Co, and Ni (Fig. 3e and f).

We conducted inductively coupled plasma atomic emission spectroscopy (ICP-OES) analysis on the acid-treated MMA-*x*-Acid samples to quantify their alloy compositions (Tables S1 and S2).

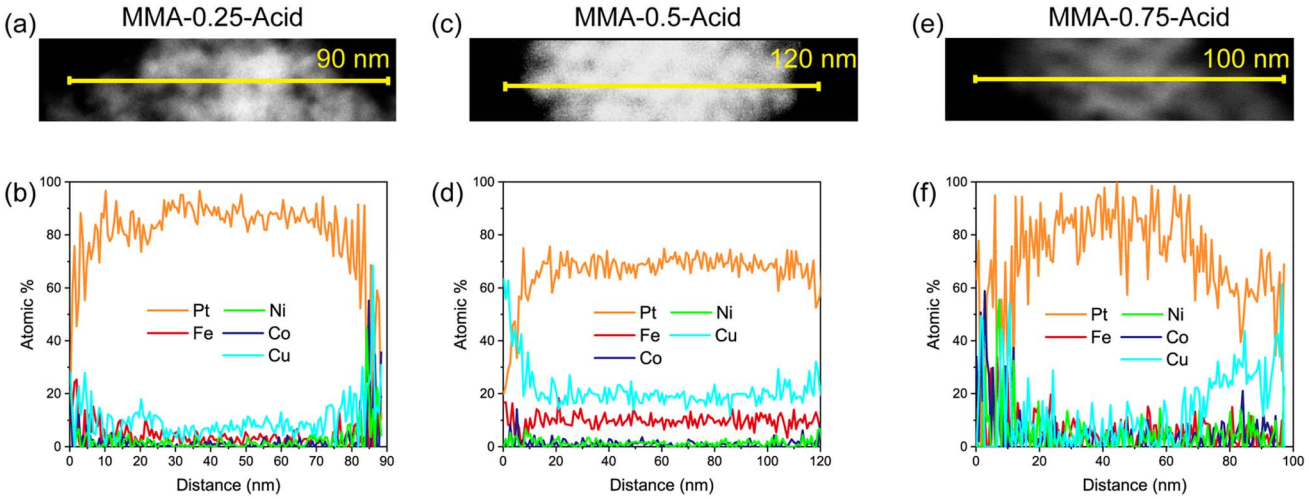

Fig. 3 HAADF-STEM line profile images and corresponding EDS spectra of (a and b) MMA-0.25-Acid, (c and d) MMA-0.5-Acid, and (e and f) MMA-0.75-Acid.

In MMA-0.25-Acid and MMA-0.5-Acid, Co and Ni were below the detection limit, consistent with the negligible amounts observed in the EDS line profiles. When the SBH concentration was increased to 0.75 M, the Co and Ni contents rose to ~0.7% and ~0.5%, respectively, which is consistent with stronger reduction promoting incorporation of transition metal elements (Fe, Co, Ni and Cu) into the ordered mesoporous framework. MMA-1-Acid exhibited similar Co and Ni contents as MMA-0.75-Acid, but a higher Cu content. For comparison, ICP-OES analysis of the as-synthesized MMA-0.75 sample revealed nearly equivalent proportions of Pt, Fe, Co, and Ni (~20–23%), with a slightly lower Fe content (~16%). Together, these results support the interpretation that the overgrown shells are enriched with Fe, Co, and Ni, and are effectively removed by acid washing. Moreover, they demonstrate that SBH concentration serves as an effective lever for tuning multimetallic composition in ordered MMAs.

Fig. 2d schematically illustrates the proposed formation mechanism of ordered cubic-like MMAs and the role of SBH concentration in alloy compositional control. Upon addition of SBH to the metal salt/KIT-6 composite, the reducing solution infiltrates the mesopores and initiates multimetallic precursor reduction (Step 1). The Pt precursor, $(PtCl_4)^{2-}$, is thermodynamically the most readily reduced among the constituents (based on relative standard reduction potentials, +0.76 V) and therefore expected to reduce first, generating Pt nuclei that seed fcc crystal growth within the KIT-6 mesopores.[11] Subsequently, Cu^{2+}, with the next higher potential (+0.34 V) and strong miscibility with Pt, can co-reduce to form a PtCu alloy. Cations of Fe^{3+} (−0.037 V), Ni^{2+} (−0.257 V) and Co^{2+} (−0.28 V) have more negative reduction potentials and typically exhibit slower kinetics, thereby are expected to reduce after initial PtCu nucleation in the presence of SBH. We postulate that newly formed Fe, Co and Ni atoms subsequently undergo a galvanic redox exchange with residual $(PtCl_4)^{2-}$ and/or Cu^{2+} species (Step 2), thereby oxidizing Fe, Co and Ni back to solvated ions.[20,28–30]

At low SBH concentration (0.25 M), the transition metal cations diffuse out of the KIT-6 mesopores, resulting in negligible incorporation of Fe, Co and Ni into the mesoporous alloy. In contrast, higher SBH concentrations (0.5–1.0 M) promote secondary reduction of Fe^{3+}, Co^{2+}, and Ni^{2+}, allowing partial incorporation of these elements into the pre-formed PtCu lattice to yield an apparent quinary alloy composition within the KIT-6 mesopores, while parallel reduction processes outside the template can produce FeCoNi-rich overgrowth shells (Step 3). During subsequent acid washing, a portion of Fe, Co, and Ni is selectively dissolved from both the near-surface regions within the mesopores and the external overgrowths, yielding ordered mesoporous particles comprising a PtCu-rich fcc solid solution that retain small amounts of Fe, Co and Ni.

Control experiments emphasize the key role of Pt in ordered mesoporous alloy formation. Fig. S10 shows that, in the absence of the Pt, the XRD pattern of the as-synthesized FeCoNiCu prepared at 0.75 M SBH exhibited diffraction peaks assignable to metallic Cu (PDF 00-001-1241) and CuO (PDF 01-078-0428), indicating partial oxidation in the Pt-free sample. The SEM image of FeCoNiCu in Fig. S11 shows uncontrolled overgrowths and poorly defined porosity features after template removal. These observations are consistent with our proposed mechanism in which early Pt reduction promotes more controlled multimetallic deposition and improved metallic-phase retention.

3.2 Electrocatalytic HER experiments

We next evaluated the electrocatalytic performance for HER in an alkaline electrolyte (1.0 M KOH). Fig. 4 and S12 show the HER polarization curves of the as-synthesized and acid-treated ordered cubic-like MMA samples, obtained from linear sweep voltammetry (LSV) experiments using a three-electrode configuration. The acid-treated MMAs consistently required lower overpotentials to drive HER compared to their untreated counterparts. For example, MMA-0.5 and MMA-0.75 required 75

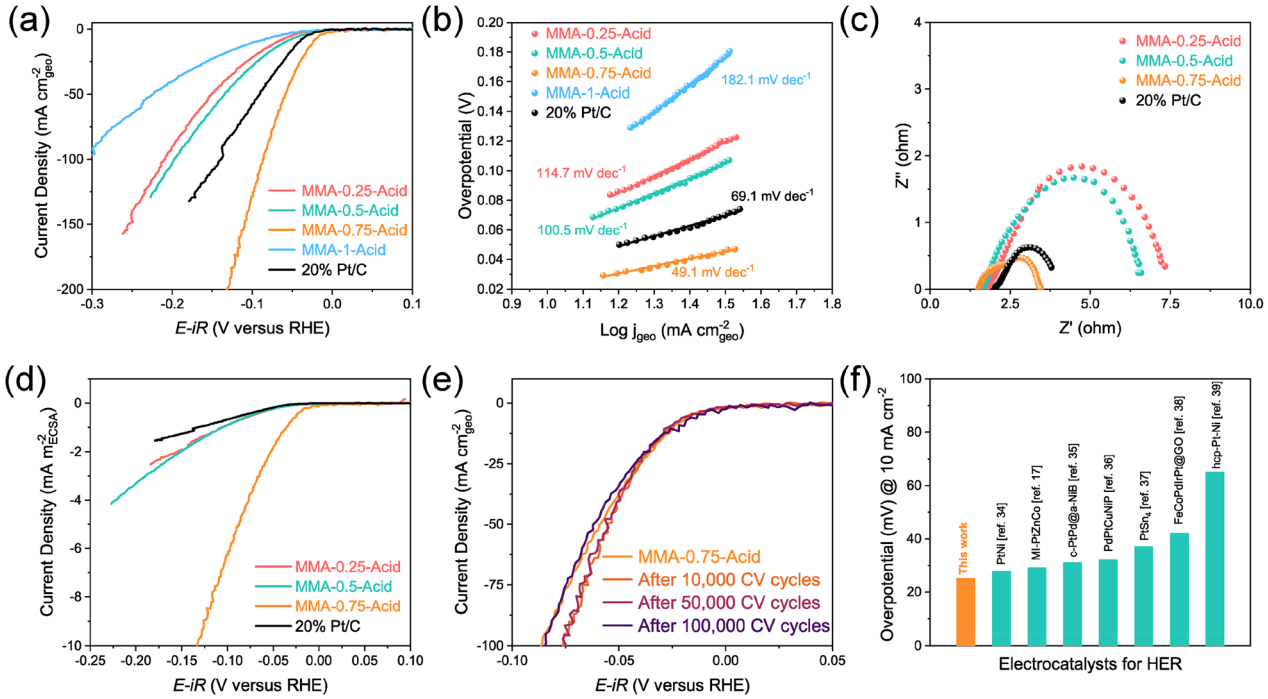

Fig. 4 (a) HER polarization curves normalized by geometric electrode area, (b) Tafel slopes, (c) EIS Nyquist plots recorded at −0.1 V *vs.* RHE, and (d) HER polarization curves normalized by ECSA for MMA-*x*-Acid samples and commercial 20 wt% Pt/C. (e) HER polarization curves of the MMA-0.75-Acid sample before and after 10 000, 50 000, and 100 000 CV cycles for ADT. (f) Comparison of the overpotential at 10 mA cm^{-2} with recently reported Pt-based catalysts (Table S3).

and 130 mV, respectively, to reach 10 mA cm^{-2}, whereas their acid-treated analogues (MMA-0.5-Acid and MMA-0.75-Acid) achieved the same current density at only 60 and 25 mV, respectively. This substantial reduction is consistent with acid washing removing FeCoNi-rich surface species and increasing the accessibility of Pt-based active sites within the mesoporous network.

Fig. 4a compares the HER polarization curves of all acid-treated MMA samples as a function of SBH concentration. Among them, MMA-0.75-Acid exhibited the best HER performance, requiring an overpotential of 85 mV to deliver 100 mA cm^{-2} in 1.0 M KOH, markedly lower than MMA-0.25-Acid (211 mV), MMA-0.5-Acid (198 mV), and MMA-1-Acid (304 mV). The enhanced activity with increasing SBH concentration from 0.25 M to 0.75 M is attributed to improved mesostructural order and optimized alloy composition, which collectively promote higher catalytic activity at Pt-rich sites alloyed with oxophilic transition metals (Table S2). In contrast, the poor performance of MMA-1-Acid likely arises from excessively rapid reduction at 1.0 M SBH, which can promote uncontrolled nucleation and coarsening into larger aggregates, leading to partial loss of mesoscale order and local pore blockage even after acid treatment (Fig. S1).

Notably, MMA-0.75-Acid outperformed both commercial 20 wt% Pt/C (43 and 139 mV at 10 and 100 mA cm^{-2}, respectively) and mesoporous pure Pt (80 mV at 10 mA cm^{-2}, Fig. S13a) at a comparable metal loading of ~40 μg cm^{-2}, underscoring the beneficial alloying effects of Pt with Cu, Fe, Co and Ni in accelerating HER kinetics in alkaline media.[11,15,16] This trend is further supported by mass activity analysis (Fig. S14), where MMA-0.75-Acid achieved a mass activity of 3.9 A mg$_{Pt}^{-1}$ at −0.1 V, which is 4.9-, 4.0-, 10.8-, and 2.7-fold higher than those of MMA-0.25-Acid (0.79 A mg$_{Pt}^{-1}$), MMA-0.5-Acid (0.98 A mg$_{Pt}^{-1}$), MMA-1-Acid (0.36 A mg$_{Pt}^{-1}$), and commercial 20 wt% Pt/C (1.44 A mg$_{Pt}^{-1}$), respectively. To exclude the influence of catalyst film thickness on mass transport, we conducted LSV measurements of commercial 20 wt% Pt/C with a lower Pt loading of ~8 μg$_{Pt}$ cm^{-2}. The HER polarization curves in Fig. S15 show that MMA-0.75-Acid exhibited higher HER activity when normalized to both geometric electrode area and Pt mass.

To further probe the HER kinetics, we analyzed the corresponding Tafel slopes as shown in Fig. 4b. MMA-0.75-Acid exhibited the smallest Tafel slope of 49.1 mV dec^{-1}, reflecting the fastest HER kinetics among the tested catalysts in alkaline media, compared with MMA-0.25-Acid (114.7 mV dec^{-1}), MMA-0.5-Acid (100.5 mV dec^{-1}), and MMA-1-Acid (182.1 mV dec^{-1}). In contrast, the control catalysts, commercial 20 wt% Pt/C (69.1 mV dec^{-1}) and mesoporous pure Pt (145.2 mV dec^{-1}, Fig. S13b), displayed higher Tafel slopes, corroborating the kinetic advantages introduced by Pt alloying with transition metals.

Further insight into charge transfer behavior was obtained from electrochemical impedance spectroscopy (EIS), presented as Nyquist plots and equivalent circuit fits in Fig. 4c and S16. MMA-0.75-Acid displayed the smallest semicircle,

corresponding to a charge transfer resistance (R_{ct}) of 0.93 Ω, which was substantially lower than those of MMA-0.25-Acid (5.18 Ω), MMA-0.5-Acid (3.33 Ω), and even commercial 20 wt% Pt/C (1.63 Ω). This minimal R_{ct} is consistent with accelerated HER charge transfer kinetics imparted by the optimized ordered mesoporous structure and multimetallic alloy composition.

We calculated the electrochemically active surface areas (ECSA) of the acid-treated MMA samples and the control catalysts, mesoporous Pt-only and commercial 20 wt% Pt/C, using hydrogen underpotential deposition (HUPD) analysis based on cyclic voltammetry (CV) measured at a scan rate of 10 mV s^{-1} (Fig. S17).[17,26] The ECSA values of the acid-treated MMA samples were lower, ranging from 10.2 to 17.0 m^2 g^{-1}, than that of commercial 20 wt% Pt/C (42.9 m^2 g^{-1}). This difference can be primarily attributed to the sub-10 nm Pt nanoparticles supported on carbon in Pt/C which provide a higher density of exposed Pt sites than the larger MMA frameworks (Fig. S18). The mesoporous Pt-only control sample exhibited the smallest ECSA value (8.1 m^2 g^{-1}), suggesting that the enhanced HER performance of mesoporous MMAs arises primarily from increased intrinsic activity of Pt-based sites rather than from an increased number of active sites.

Despite their lower ECSA, the ECSA-normalized HER polarization curves in Fig. 4d reveal that at −0.10 V, MMA-0.75-Acid delivered a current density of 6.3 mA m_{ECSA}^{-2}, which is nearly an order of magnitude higher than that of Pt/C (0.67 mA m_{ECSA}^{-2}), demonstrating markedly enhanced intrinsic activity. Compared with the mesoporous Pt control sample, MMA-0.75-Acid exhibited a current density of 1.82 mA m_{ECSA}^{-2}, 6.5-fold higher than that of mesoporous Pt (0.28 mA m_{ECSA}^{-2}) at −0.05 V. We attribute the improvement to alloying-induced electronic modulations of Pt site, optimizing hydrogen adsorption energetics and lowering kinetic barriers along the alkaline HER pathway.[16,31]

Earlier EDX and ICP-OES analyses show that the acid-treated MMAs have a PtCu-rich composition with minor amounts of Fe, Co, and Ni. Cu, the major alloying element, has a filled 3d orbital with a d-band center typically well below the Fermi level.[32] We postulate that alloying Pt with Cu likely downshifts the Pt d-band center relative to the Fermi level, thereby weakening the adsorption energy of hydrogen intermediates to a more moderate value.[7] This interpretation is consistent with the Sabatier principle, which states that moderate binding energy of hydrogen intermediates facilitates balanced adsorption and desorption and thereby promotes HER activity.[13]

We performed X-ray photoelectron spectroscopy (XPS) on as-prepared MMA-0.75-Acid and mesoporous Pt to probe near-surface electronic states of Pt as shown in Fig. S19a. Compared with the Pt-only control sample, the Pt 4f spectrum of MMA-0.75-Acid exhibited a negative shift of ∼0.3 eV towards lower binding energy level, suggesting that Pt sites in MMA-0.75-Acid accept electrons from neighboring transition metals and adopt an electron-rich structure.[7,33] It is well established that such an electron-rich Pt environment can facilitate hydrogen desorption, thereby enhancing HER activity.[17] In addition, the low intensity and noisy Co 3p and Ni 3p XPS signals indicate low Co and Ni contents in MMA-0.75-Acid, consistent with the ICP-OES and EDX results (Fig. S19c and d).

We evaluated the HER durability of ordered MMA using accelerated durability tests (ADT), in which MMA-0.75-Acid was subjected to CV over 100 000 cycles. Fig. 4e presents the corresponding HER polarization curves recorded after 10 000, 50 000, and 100 000 cycles. MMA-0.75-Acid exhibited an apparent electrochemical activation between 10 000 and 50 000 cycles, after which the HER polarization curve remained highly similar to that of the initial state before ADT. SEM analysis performed after ADT confirmed that the mesoporous architecture of MMA-0.75-Acid was retained, demonstrating robust structural stability (Fig. S20). In contrast, the control Pt/C catalyst displayed notable degradation, with the overpotential at 10 mA cm^{-2} increasing by 22 mV after 100 000 cycles (Fig. S21).

XPS measurements of MMA-0.75-Acid after 100 000 ADT cycles revealed negligible changes in the Pt 4f binding energy positions relative to as-prepared sample, indicating that the Pt sites remained electron-rich during prolonged electrochemical operation (Fig. S19b). The disappearance of Co and Cu XPS signals suggests that these two constituent metals were leached during ADT cycling (Fig. S19d and f). In contrast, the Fe 3p spectrum (Fig. S19c) exhibited a negative shift towards lower binding energy, while Ni 3p spectrum (Fig. S19e) showed a positive shift, suggesting electron transfer from Ni to Fe after ADT.[34] Despite these compositional changes, the ECSA of MMA-0.75-Acid after ADT remained comparable (9.92 m^2 g^{-1}) to that of the neat sample, highlighting the durability of the active Pt sites in the ordered MMA framework. Finally, to contextualize the HER performance, Fig. 4f compares the overpotentials at 10 mA cm^{-2} of recently reported Pt-based catalysts for alkaline HER (Table S3).[17,35–40] MMA-0.75-Acid ranks among the most active and durable materials, underscoring its promise as a highly efficient electrocatalyst for alkaline hydrogen evolution.

4 Conclusions

In summary, we establish a one-pot nanocasting-reduction strategy that enables the synthesis of single-phase fcc ordered multimetallic alloys with an inverse bicontinuous cubic architecture. By tuning the SBH concentration, we simultaneously control mesostructure periodicity and fidelity, as well as the incorporation of oxophilic transition metals through a coupled sequence of PtCu nucleation, galvanic exchange and selective oxidation, and SBH-driven re-reduction. Higher SBH concentrations generate FeCoNi-rich overgrowth shells that are selectively removed by acid etching, yielding a PtCu-rich ordered mesoporous framework with low level incorporation of Fe, Co and Ni that electronically modifies the Pt lattice. The optimized MMA-0.75-Acid catalyst combines high structural order with alloying-induced electronic modulation of Pt sites, delivering enhanced intrinsic HER activity and excellent durability over 100 000 CV cycles while retaining an electron-rich electronic structure and stable ECSA, thereby outperforming commercial Pt/C. These results demonstrate that controlled low-level alloying of PtCu frameworks within ordered mesoporous networks can imprint durable electronic effects on Pt active sites, offering

a highly effective design principle for electrocatalysis. We envision that the SBH-tuned one-pot nanocasting method provides a versatile synthetic platform for creating ordered mesoporous multimetallic solid solution alloys with programmable compositions and morphologies for catalysis, sensing and plasmonic applications.

Author contributions

C. Xia: writing – original draft, writing – review & editing, visualization, validation, methodology, investigation, formal analysis, conceptualization, data curation. J. Ma: writing – original draft, writing – review & editing, visualization, validation, methodology, investigation, formal analysis, conceptualization, data curation. Q. Chen: writing – review & editing, investigation, formal analysis. Y. Y. Tay: writing – review & editing, investigation, formal analysis. L. H. Wong: writing – review & editing, supervision, formal analysis. K. W. Tan: writing – review & editing, validation, supervision, project administration, funding acquisition, formal analysis, conceptualization, data curation.

Conflicts of interest

There are no conflicts to declare.

Data availability

The data supporting this article have been included as part of the supplementary information (SI). Supplementary information is available. See DOI: https://doi.org/10.1039/d5ta09402j.

Acknowledgements

This work was supported by the Singapore Ministry of Education AcRF Tier 2 grant (MOE-T2EP50221-0017). This work made use of research facilities at the Facility for Analysis, Characterization, Testing and Simulation (FACTS), Nanyang Technological University, Singapore. We also gratefully thank Dr Weiling Liu, Dr Teddy Salim, Dr Jo-Chi Tseng and Qian Xin of Nanyang Technological University for their kind experimental assistance and helpful discussions. The authors used ChatGPT (OpenAI) solely for assistance to refine language and improve readability. All text was reviewed and edited by the authors, who take full responsibility for the content of the publication.

Notes and references

1 H. Lv and B. Liu, *Chem. Soc. Rev.*, 2024, **53**, 11321–11333.
2 Y. Zou, X. Zhou, J. Ma, X. Yang and Y. Deng, *Chem. Soc. Rev.*, 2020, **49**, 1173–1208.
3 W. Li, J. Liu and D. Zhao, *Nat. Rev. Mater.*, 2016, **1**, 1–17.
4 E. M. Farber, N. M. Seraphim, K. Tamakuwala, A. Stein, M. Rücker and D. Eisenberg, *Science*, 2025, **390**, eadn9391.
5 V. Malgras, H. Ataee-Esfahani, H. Wang, B. Jiang, C. Li, K. C.-W. Wu, J. H. Kim and Y. Yamauchi, *Adv. Mater.*, 2016, **28**, 993–1010.
6 Y. Wang, H. Lv, L. Sun and B. Liu, *ACS Nano*, 2021, **15**, 18661–18670.
7 Y. Kang, O. Cretu, J. Kikkawa, K. Kimoto, H. Nara, A. S. Nugraha, H. Kawamoto, M. Eguchi, T. Liao, Z. Sun, T. Asahi and Y. Yamauchi, *Nat. Commun.*, 2023, **14**, 4182.
8 Y. Li, H. Yao, L. Sun, S. Han, X. Xu, G. Fan and B. Liu, *Sci. China:Chem.*, 2025, **68**, 3295–3301.
9 L. Sun, H. Lv, J. Xiao and B. Liu, *Adv. Mater.*, 2024, **36**, 2402767.
10 L. Sun and B. Liu, *Acc. Chem. Res.*, 2025, **58**, 2306–2316.
11 R. Nandan, H. N. Nam, Q. M. Phung, H. Nara, J. Henzie and Y. Yamauchi, *J. Am. Chem. Soc.*, 2025, **147**, 18651–18661.
12 Y. Wang, X. Zhang, H. He, J. Chen and B. Liu, *Adv. Energy Mater.*, 2024, **14**, 2303923.
13 J. Zhang, H. B. Yang, D. Zhou and B. Liu, *Chem. Rev.*, 2022, **122**, 17028–17072.
14 J. Greeley and M. Mavrikakis, *Nat. Mater.*, 2004, **3**, 810–815.
15 D. Wu, K. Kusada, Y. Nanba, M. Koyama, T. Yamamoto, T. Toriyama, S. Matsumura, O. Seo, I. Gueye, J. Kim, L. S. Rosantha Kumara, O. Sakata, S. Kawaguchi, Y. Kubota and H. Kitagawa, *J. Am. Chem. Soc.*, 2022, **144**, 3365–3369.
16 R. Nandan, H. Nara, H. N. Nam, Q. M. Phung, Q. P. Ngo, J. Na, J. Henzie and Y. Yamauchi, *Adv. Sci.*, 2024, **11**, 2402518.
17 Y. Wang, H. Lv, L. Sun, F. Jia and B. Liu, *Adv. Energy Mater.*, 2022, **12**, 2201478.
18 S. C. Warren, L. C. Messina, L. S. Slaughter, M. Kamperman, Q. Zhou, S. M. Gruner, F. J. DiSalvo and U. Wiesner, *Science*, 2008, **320**, 1748–1752.
19 Z. Li, K. Hur, H. Sai, T. Higuchi, A. Takahara, H. Jinnai, S. M. Gruner and U. Wiesner, *Nat. Commun.*, 2014, **5**, 3247.
20 N. Kar, M. McCoy, J. Wolfe, S. L. A. Bueno, I. H. Shafei and S. E. Skrabalak, *Nat. Synth.*, 2023, **3**, 175–184.
21 H. Lv, Y. Wang, L. Sun, Y. Yamauchi and B. Liu, *Nat. Protoc.*, 2023, **18**, 3126–3154.
22 C. D. Cowman, E. Padgett, K. W. Tan, R. Hovden, Y. Gu, N. Andrejevic, D. Muller, G. W. Coates and U. Wiesner, *J. Am. Chem. Soc.*, 2015, **137**, 6026–6033.
23 L. Sun, H. Lv, J. Feng, O. Guselnikova, Y. Wang, Y. Yamauchi and B. Liu, *Adv. Mater.*, 2022, **34**, 2201954.
24 H. Lv, H. Qin, K. Ariga, Y. Yamauchi and B. Liu, *Angew. Chem., Int. Ed.*, 2022, **61**, e202116179.
25 F. Kleitz, S. H. Choi and R. Ryoo, *Chem. Commun.*, 2003, 2136–2137.
26 Z. Zhao, H. Liu, W. Gao, W. Xue, Z. Liu, J. Huang, X. Pan and Y. Huang, *J. Am. Chem. Soc.*, 2018, **140**, 9046–9050.
27 K. W. Tan, H. Sai, S. W. Robbins, J. G. Werner, T. N. Hoheisel, S. A. Hesse, P. A. Beaucage, F. J. DiSalvo, S. M. Gruner, M. Murtagh and U. Wiesner, *RSC Adv.*, 2015, **5**, 49287–49294.
28 R. L. Calabro, G. L. Longstaff, E. M. Tang, V. M. Xiao, A. S. Zammit, F. W. Zhang, E. A. Nagelli, P. H. Chapman, T. J. Lawton, M. A. Allen, A. R. Losch, J. L. Palmer, A. D. Ciampa, I. Z. Burpeau, V. M. Lucian, G. T. Mandes, S. F. Bartolucci, J. A. Maurer and F. J. Burpo, *ACS Appl. Mater. Interfaces*, 2025, **17**, 26854–26870.

29 S. Funo, F. Sato, Z. Cai, G. Chang, Y. He and M. Oyama, *ACS Omega*, 2021, **6**, 18395–18403.
30 S. L. Zhang, X. F. Lu, Z. Wu, D. Luan and X. W. Lou, *Angew. Chem., Int. Ed.*, 2021, **60**, 19068–19073.
31 G. Feng, F. Ning, J. Song, H. Shang, K. Zhang, Z. Ding, P. Gao, W. Chu and D. Xia, *J. Am. Chem. Soc.*, 2021, **143**, 17117–17127.
32 Z. W. Lu, S.-H. Wei and A. Zunger, *Phys. Rev. B: Condens. Matter Mater. Phys.*, 1992, **45**, 10314–10330.
33 Z. W. Chen, J. Li, P. Ou, J. E. Huang, Z. Wen, L. Chen, X. Yao, G. Cai, C. C. Yang, C. V. Singh and Q. Jiang, *Nat. Commun.*, 2024, **15**, 359.
34 H. Zhu, S. Sun, J. Hao, Z. Zhuang, S. Zhang, T. Wang, Q. Kang, S. Lu, X. Wang, F. Lai, T. Liu, G. Gao, M. Du and D. Wang, *Energy Environ. Sci.*, 2023, **16**, 619–628.
35 Z. Zhang, G. Liu, X. Cui, B. Chen, Y. Zhu, Y. Gong, F. Saleem, S. Xi, Y. Du, A. Borgna, Z. Lai, Q. Zhang, B. Li, Y. Zong, Y. Han, L. Gu and H. Zhang, *Adv. Mater.*, 2018, **30**, 1801741.
36 K. Deng, T. Ren, Y. Xu, S. Liu, Z. Dai, Z. Wang, X. Li, L. Wang and H. Wang, *J. Mater. Chem. A*, 2020, **8**, 8927–8933.
37 Z. Jia, K. Nomoto, Q. Wang, C. Kong, L. Sun, L. Zhang, S. Liang, J. Lu and J. J. Kruzic, *Adv. Funct. Mater.*, 2021, **31**, 2101586.
38 G. Li, C. Fu, W. Shi, L. Jiao, J. Wu, Q. Yang, R. Saha, M. E. Kamminga, A. K. Srivastava, E. Liu, A. N. Yazdani, N. Kumar, J. Zhang, G. R. Blake, X. Liu, M. Fahlman, S. Wirth, G. Auffermann, J. Gooth, S. Parkin, V. Madhavan, X. Feng, Y. Sun and C. Felser, *Angew. Chem., Int. Ed.*, 2019, **58**, 13107–13112.
39 S. Gao, S. Hao, Z. Huang, Y. Yuan, S. Han, L. Lei, X. Zhang, R. Shahbazian-Yassar and J. Lu, *Nat. Commun.*, 2020, **11**, 2016.
40 Z. Cao, Q. Chen, J. Zhang, H. Li, Y. Jiang, S. Shen, G. Fu, B. Lu, Z. Xie and L. Zheng, *Nat. Commun.*, 2017, **8**, 15131.